Communications Earth & Environment https://doi.org/10.1038/s43247-026-03228-1

Article in Press

Reactivation of basement faults by deep fluids during the 2017 Changdao earthquake swarm, Eastern China

Received: 6 May 2025

Accepted: 16 January 2026

Cite this article as: Wang, P., Wang, B., Peng, Z. *et al.* Reactivation of basement faults by deep fluids during the 2017 Changdao earthquake swarm, Eastern China. *Commun Earth Environ* (2026). https://doi.org/10.1038/s43247-026-03228-1

Peng Wang, Baoshan Wang, Zhigang Peng & Xinglin Lei

Reactivation of basement faults by deep fluids during the 2017 Changdao earthquake swarm, Eastern China

Peng Wang[1], Baoshan Wang[2,3], Zhigang Peng[4], Xinglin Lei[5]

1, Shandong Institute of Petroleum and Chemical Technology, Dongying, 257061, China

2, Mengcheng National Geophysical Observatory, University of Science and Technology of China, Mengcheng, 233500, China

3, State Key Laboratory of Precision Geodesy, School of Earth and Space Sciences, University of Science and Technology of China, Hefei, 230026, China

4, School of Earth and Atmospheric Sciences, Georgia Institute of Technology, Atlanta, 30315, USA

5, National Institute of Advanced Industrial Science and Technology, Geological Survey of Japan, Tsukuba, 305-0045, Japan

Corresponding author: Baoshan Wang (bwgeo@ustc.edu.cn)

Abstract: Ancient basement faults within plate interiors may be reactivated by external forces, generating intraplate seismicity. However, the driving mechanisms remain unclear. The 2017 Changdao earthquake swarm in the Bohai Bay Basin, eastern China, provides an opportunity to investigate such processes. A high-resolution earthquake catalog, constructed using matched filter detection and waveform-based relocation, reveals that the swarm occurred at 7-13 km depth along an X-shaped fault network, with migration following sqrt(t) diffusion ($D=0.08 – 1.2\ m^2\ s^{-1}$). High b-values and external forcing rate, and substantial isotropic components (13-38%) in the moment tensors indicate fluid involvement. Combined with low V_P/V_S ratios and proximity to CO_2-rich hydrocarbon fields, we propose a fault-valve model where highly compressible fluids episodically breach fault intersections, triggering transient crack opening and swarm migration. This study reveals how deep fluids reactivate ancient basement faults in intraplate regions, and provides new insights for seismic hazard assessment in hydrocarbon-bearing basins.

Introduction

Faults are ubiquitous in the Earth's crust and play crucial roles in controlling the mechanical properties of the crust and its seismogenic behaviors[1,2]. Crustal faults can be roughly categorized into basement faults that were formed during earlier tectonic phases, and neotectonic faults, which were primarily developed within sedimentary formations during recent geological activities[3]. Most neotectonic and basement faults remain quiescent for many years, but they can be reactivated by external stress perturbations such as fluid flow, aseismic slip, or other nearby earthquakes[4,5]. The reactivation of dormant faults, especially deep basement faults, may trigger moderate-size to large-magnitude events[6,7,8,9]. Understanding activation of ancient basement faults provides important insights into the geological evolution and seismic hazard assessment, especially at intraplate regions[8,9,10,11,12,13].

Fluids are known to play an appreciable role in crustal fault reactivation, which reduces the effective stress and/or fault strength and further induces seismic activities[14,15,16,17]. A common manifestation of fluid-driven fault reactivation is earthquake swarms, which refer to sequences that are closely clustered with clear migrations in space and time without a dominant mainshock[18,19,20,21]. The majority of earthquake swarms occurred at the shallow crust near volcanic and/or geothermal systems, which is generally attributed to the fluid migration from either natural source[21,22,23,24,25] or industrial injections[26,27] and possibly aseismic slips along active fault zones[28,29,30].

Compared to shallow earthquake swarms, research on swarms reactivated along deep basement faults is challenging due to the scarcity of observations, limited resolution of basement fault geometry, and complex stress and fluid interactions[7,31,32,33]. Recent seismological and geodetic studies of earthquake swarms in well-monitored regions such as the Noto Peninsula, Japan, have provided insights into the physical mechanism of fault reactivation driven by deep fluids and aseismic slip[8,9,16,17,34]. However, how the basement faults respond to deep fluid pressure and other external stress perturbations is not well understood, especially at intraplate regions with relatively sparse instrumentations[28,35,36,37].

In February 2017, an earthquake swarm initiated in the Changdao area in the eastern edge of the Bohai Bay Basin, eastern China. Multiple earthquake swarms have been recorded in this region, including earthquake swarms that occurred in 1976, 2013, and most prominently in 2017. In a broader context, this region has hosted intense historic and current seismicity in the past, with the largest M7 event in 1548. The 2017 swarm lasted from February 14 to August 2017. It stands out as the most prominent one in terms of duration, frequency, and maximum magnitude, surpassing previous events (Figure 1). The Changdao area hosts a complex fault system including multiple shovel-shaped basement faults in the middle crust, most of which merge with the basin basement at a depth of 7-16 km, and the conjugate shear fault system with a flower-like structure in the shallow crust[3]. Some studies imaged the middle and lower crust as low-velocity zones, indicating possible connections between the swarm evolution and fluids from deep sources[38,39]. However, most previous studies were based on the standard earthquake catalog from the China Earthquake Networks Center (CENC), which has location precisions on the order of a few kilometers and is likely incomplete, especially for lower magnitude events. Hence, the precise spatiotemporal evolution of seismicity, the 3D fault structure hosting the swarm, and the underlying physical mechanisms remain ambiguous.

In this paper, we constructed a high-resolution earthquake catalog using matched-filter event detection[40,41] and waveform cross-correlation-based double-difference relocation[42,43] techniques. The refined catalog depicts a complex fault system and shows a clear spatio-temporal evolution consistent with a fluid-driven mechanism. Combining evidence from different observations, we proposed a mechanism of deep fluid-triggered fault reactivation, which may provide more insights into the interaction between earthquake swarms and deep fluids at intraplate regions.

Results

General features of the high-resolution earthquake catalog

Using the matched filter technique and a waveform cross-correlation-based location procedure (see the Method section for details), we obtained two new catalogs: a matched-filter-only (MFO) catalog (without relocation) containing 11,411 events (Supplementary Data 1), 6 times more than the number (1804) provided by CENC, and a matched-filter-relocated (MFR) catalog, a subset of MFO, containing 2,142 events (Supplementary Data 2)[45]. The magnitudes of the newly detected events were primarily concentrated between 0.0 and 1.0 (Figure 2a). The corresponding magnitude of completeness Mc, obtained with the maximum curvature method[46], decreases from 1.1 in the original CENC catalog to 0.8 in the MFO catalog (Figure 2b). The median location errors of MFR, indicated by 80% fitting errors, were less than 100 m in both the horizontal and depth directions (Supplementary Figure S3). Such a high location precision enables the depiction of detailed structures as minor sub-faults.

The 2017 earthquake sequence during this period can be roughly divided into three stages according to the seismicity rate variation in the MFO catalog (Figure 2a). The first stage started on February 14, 2017, and ended just before the largest M_L4.5 earthquake on March 3, 2017. The second stage was the most energetic, beginning with the M_L4.5 earthquake and ending on May 7, 2017. The final stage lasted from May 8 to May 31, 2017.

The subsequent analysis was based primarily on the relocated MFR catalog, where the swarm exhibited an overall NWW-SEE orientation (Figure 3a) in the horizontal plane. However, further zoomed distribution indicates that most earthquakes were concentrated in the central area along a NEE linear trend (Figure 3a), which was not evident in the CENC catalog (Figure 1). The relocated events delineated a complex X-shaped fault architecture, including a shovel-shaped listric fault (F1), an oppositely dipping fault (F2), and several secondary faults (Figure 3b). Fault F1 was characterized by a steeply inclined upper segment and a flatter lower segment, intersected by F2. The two faults exhibited dips of approximately 70° toward the southeast and northwest, forming an intersecting fracture zone (Figure 3b). Additionally, several secondary faults delineated by relocated seismicity branched off from the major faults (F1, F2), forming a forked fault geometry (Figure 3b). The focal depths ranged from 5 to 15 km, with the majority clustered at depths of 7 to 13 km (Figure 3b), and side-view along the NE direction shows the epicenters were primarily clustered within an area of ~4 km long and 3 km deep (Figure 3c). By further zooming in on this region, we can clearly identify the earthquake migration process, which started from the northeast and migrated to the southwest horizontally over a period of 3.5 months. These spatial patterns were further illustrated in the three-dimensional (3D) view (Figure 4) and offered a detailed depiction of the complex fault architecture.

Focal mechanisms

We inverted moment tensors for six events with $M_L \geqslant 3.5$ using the Cut-and-Paste (CAP) method[47]. Those events were recorded with adequate azimuthal coverage, and the focal mechanism solutions explained the waveforms well (Supplementary Table S1). Focal mechanisms for 179 smaller (M_L 2.0-3.4) earthquakes were also determined through P-wave first-motion polarity analysis[48].

All six $M_L \geqslant 3.5$ events were dominated by strike-slip (Figure 3), and focal mechanism solutions of all 179 smaller (M_L 2.0-3.4) earthquakes (Supplementary Figure S4, Supplementary Data 1) were predominantly strike-slip, with a few events showing normal faulting characteristics. The largest event (M_L 4.5) had one nodal plane solution of 321°/59°/3°, with a centroid depth of 9.3 km (2.1 km shallower than the MFR hypocenter depth 11.4 km). Moment tensor analysis revealed that three of the six $M_L \geq 3.5$ events exhibited robust positive isotropic (ISO) components even after uncertainty corrections: 15±4% for the M_L 4.5 on March 3, 38±13% for the M_L 3.5 on March 16, and 13±4% for the M_L 4.1 on March 27 (Supplementary Table S1, Supplementary Figure S2, S5). While the compensated linear vector dipole (CLVD) components were generally negligible (e.g., -0.03±0.03 for the M_L 4.5 event). Substantial ISO components, combined with the dominant double-couple (DC) slip mechanisms, suggest predominantly shear-tensile ruptures with fault opening[49].

Based on the focal mechanisms of all $M_L \geq 2.0$ earthquakes, we inverted the stress orientations using an iterative stress inversion method[50]. The results indicated orientation and plunge of the maximum principal stress axis (σ1) are 103.1° and 6.1°, respectively. The inverted direction of the maximum horizontal principal stress was nearly east-west (102° ± 1°), consistent with the orientation (101.4°) of the maximum regional horizontal stress[51].

Spatio-temporal Migration of Earthquake Swarms

The earthquake swarm initiated from the base of the northeastern segment of the fault system (Figures 3a, 4). During Stage I, the initial seismic cluster occurred at depths of 10.5 km to 12 km mainly in the intersection zones between the shovel-shaped basement fault (F1) and the oppositely dipping fault (F2) (Figures 3d, 4, and S6a). Following the initial active period (12 days), the activity paused for 5 days until the occurrence of the largest M_L 4.5 event, at the base of the intersection between F1 and F2 on March 3, 2017 (Figure 2). After that, earthquakes gradually migrated to the upper segments of F1 and F2 (in Stage II) (Supplementary Figure S6b). Subsequently, seismic activity increased sharply after an M_L 3.6 earthquake on March 14, 2017 (from ~90 to ~179 events/day, Figure 2a), and earthquakes migrated southwestward in the central segment (Figure 4 and Supplementary Figure S6c). Simultaneously, earthquakes also occurred along the lower segment of F1 and secondary faults along F1 (Figure 3b and Supplementary Figure S6c). Several swarm-like seismic clusters successively occurred following relatively large earthquakes, such as an M_L 3.5 event on April 8 and an M_L 3.3 event on May 2 (Figure 5). Finally, the seismic activity began to decay substantially from May 8 (in Stage III), but the hypocenters continued to expand until encompassing the entire fault system. The migration process of the whole swarm lasted for 105 days. More detailed spatio-temporal evolution is presented in Figure 4, Supplementary Figure S6 and Supplementary Movie S1.

As mentioned before, the Changdao swarm exhibited systematic hypocentral migration where the distance between the activity front and the initial earthquake (2017-02-14 00:05:58) gradually increased with time (Figure 5a and Supplementary Figure S6a). The migration of activity front can be approximately fitted with the fluid diffusion equation[19,31,52,53] (See Methods). The overall migration front for the entire swarm was generally behind the curve with a diffusivity of 1.2 $m^2 s^{-1}$ (Figure 5a). Besides the overall migration pattern, there are several visible sub-migrations, which can be fitted with diffusivities ranging from 0.5 to 1.0 $m^2 s^{-1}$ (Figure 5a). Similar migration characteristics were also observed across distinct fault segments, and the migration fronts in the southeast and northwest regions (SR and NR in Figure 3a) were fitted with diffusivities of 0.5 $m^2 s^{-1}$ and 0.3 $m^2 s^{-1}$ (Figures 5c, 5d), respectively. In comparison, the seismicity in the central region (CR in Figure 3a) followed a similar pattern with a much smaller diffusivity of 0.08 $m^2 s^{-1}$ (Figure 5b), and the sub-migration diffusivities in the central region during different time periods were 0.17 $m^2 s^{-1}$ and 0.6 $m^2 s^{-1}$, respectively. The cumulative seismicity plot (Figure 5a) showed that the earthquake surges and dense earthquake clustering were typically triggered by relatively large events, such as the M_L 4.5 event on March 3, the M_L

3.6 event on March 14, and the M_L 3.5 event on April 8. The seismicity shortly following these large events did not follow the typical sqrt(t) migration pattern, suggesting a different driving mechanism.

Discussion

Fluid diffusion, aseismic slip, and cascade stress transfer are widely recognized driving mechanisms for earthquake swarms[25,53,54,55] and other types of earthquake sequences**Error! Reference source not found.**. Recent studies found that these physical mechanisms often work in concert to drive earthquake swarms[8,21,29,30,56]. To quantify the role of aseismic slip in the 2017 Changdao swarm, we first examined data from the nearest GNSS station (YTA, Figure 1) but detected no robust aseismic signals (Supplementary Figure S8), possibly due to strong ocean-related noise and long distance (~ 80 km) from the swarm. Nevertheless, the systematic sqrt(t) type migration (Figure 5) provided evidence of fluid pressure diffusion, as observed in other sequences[20,22,31,57,58,59,60]. In addition, cascade stress transfer often interacts with fluid pressure, which likely expands the swarm's spatial range.

This interplay between earthquakes is further investigated with the time-dependent epidemic-type aftershock sequence (ETAS) model[61,62,63]. The modeled time-varying background rate $\lambda_0(t)$ revealed that external forcing accounts for ~63% of swarm activity, with the remainder attributable to Omori-type self-triggered activity (Figure 6a), indicating that ~63% of the earthquakes were forced externally and the most likely agent is mid-crustal fluids. Initially, external forcing contributed 47.5% in Stage I suggesting a balance between fluids and seismic triggering effects; it then rose to 82.9% in the most active period of Stage II (Figures 2, 5), highlighting the dominance of fluid-driven processes. The Omori law parameter α varied from 0.921 to 1.334, and decreased to 0.647, indicating weaker aftershock productivity than tectonic sequences (Figure 6b). The results from ETAS modeling are consistent with the sqrt(t)-type migration features (Figure 5).

In the area of fluid-induced seismicity in the Western Canada Sedimentary Basin[64], the positive component of the ISO component was observed to be larger than 15%. Prominent ISO component observed in our study (Supplementary Table S1, Supplementary Figures S2, S5) supports a fluid-overpressure model[49], wherein trapped fluids build overpressure to reduce effective normal stress on the fault plane, facilitating tensile or mixed-mode faulting rather than pure shear slip.

Although influenced by stress, fault heterogeneity, and fluid interactions[18,46], relative b-values in the Changdao swarm, ranging from 0.9 to 1.5 across the swarm and different stages, consistently exceeded the regional background of 0.74 (Supplementary Figures S9a, S9b). Spatially, the b-value (1.28) was higher around the main fault planes and multi-oriented small-fault zones, while lower b-values (0.91) were observed in the southwestern part (Supplementary Figure S9c). The evolution of b-value may reflect the spatiotemporal evolution of pore pressure and its role in controlling fault rupture.

Seismic tomography provided another independent evidence for the fluid-overpressure mechanism, as it can delineate zones of fluid upwelling and fracture networks[65,66]. Using Qu et al. (2021) velocity model in this region[39], we found that the swarm concentrated in a low-V_P/V_S zone, and laterally bounded by areas with higher V_P/V_S ratios (Figure 7a). This observation is generally consistent with another tomographic imaging study in the same region[67], and other swarm sequences in California[68,69] , Japan[8,70,71,72] and Iceland[73,74]. Low V_P/V_S ratios generally indicate presence of special mineral types such as quartz[75], gas-filled or unsaturated cracks, large-aspect-ratio (0.01~0.1) water-filled fractures, or elevated heat flow[76,77,78], with CO_2 further reducing the V_P/V_S ratios, mainly through changes in the compressibility[65].

Geochemical evidence showed persistent deep-sourced H_2 and CO emissions in Changdao Island, with CO_2-supersaturated soils[Error! Reference source not found.]. Since the mafic basalt flow in ~2 Ma, the Changdao area has undergone multiple periods of deep-source CO_2-rich fluid activity[Error! Reference source not found.]. These CO2-rich fluids likely originate from the Big Mantle Wedge (BMW; Figure 6c), driven by Pacific Plate stagnation and dehydration[80,,81] (Figure 6c), and then migrate up along pre-existing fractures[67,Error! Reference source not found.]. Here we hypothesized that deep CO2-rich fluids migrated up through a main pathway (the low V_P/V_S zone) following pre-existing fracture network, driving the Changdao swarm sequence.

The swarm was centered on the intersection of a low-angle listric basement fault (F1) and a steeply dipping reverse fault (F2) at depths of 9 - 12 km, above the brittle-ductile transition layer (~12 - 16 km)[82,83], with negligible seismicity below low-permeability F1 acting as a caprock on top of a deep reservoir[29]. This geometry supported a fault-valve mechanism[4,6,8,21,22,24,29,84], where fluid accumulated beneath the low-permeability F1 until reaching a critical threshold, triggering rupture at the F1-F2 intersection and creating transient permeable pathways for upward migration into overlying faults along branching faults.

During the early stage, fluid diffusion followed a high-permeability migration front, with a peak diffusivity of 1.2 $m^2 s^{-1}$, consistent with overpressure-driven reactivation at the F1 – F2 intersection[6,85,86] and transient permeability enhancement due to new fractures[30,57], a pattern mirrored in the initial rise of ETAS background forcing (Figure 6b). After the largest M_L 4.5 event, diffusivity decreased to ~1.0 $m^2 s^{-1}$ and then to ~0.5 $m^2 s^{-1}$ following subsequent larger events, as expected in a fault-valve system where rupture temporarily increases permeability, followed by a relaxation/healing process that potentially reduce permeability[6,8,84]. These variations aligned with fluid-driven swarms in Long Valley Caldera[31] and Weiyuan shale-gas region[26,59,87], where high initial diffusivity rates decay as open fractures close.

The most active F1-F2 intersection exhibited the lowest diffusivity (0.08 $m^2 s^{-1}$) compared with the southeastern (SR ~0.5 $m^2 s^{-1}$) and northwestern (NR ~0.3 $m^2 s^{-1}$) segments (Figures 3, 5), likely due to localized stress concentration closing fractures and inhibiting fluid mobility in high-stress environments[89]. This was supported by lower stress drops at the intersection than in adjacent segments[88], indicating that fluid overpressure reduced effective normal stress for minimal stress release and fault reactivation with limited energy dissipation[85,86]. In addition, persistently high b-values (>1.0) (Supplementary Figure S9c) suggest abundant small ruptures in a weakened and likely fluid-saturated area.

The asymmetry between SR and NR may stem from differing fracture connectivity or stress perturbations. The forked fault geometry, combined with the exponentially decaying permeability with depth[90], suggested that fluids were first trapped and accumulated near the low-permeability intersection and migrated upward primarily through fracture networks bounded by low-permeability barriers[91,92]. Once overpressure reached a critical threshold, fluids then migrated along the upper and lower branches to secondary systems. These diffusivities aligned with similar-depth fluid-driven swarms, including Yellowstone[23] (1.5 m² s^{-1} at 8 – 11 km), Noto Peninsula[16,93] (0.09 – 200 m² s^{-1} or 0.02 – 1 m² s^{-1} at 5 – 20 km), Tengchong volcanic region[21] (0.02 – 40 m² s^{-1} at 5 – 15 km), and granite fluid-injection experiments[94] (0.1 – 100 m² s^{-1}). The fault-valve dynamics and permeability variations drive the swarm's evolution and underscore the role of fluid overpressure in basement fault reactivation.

Recent studies[95,96] also found elevated background rates during waste-water injections and volcanic unrests can affect the system's response to external stress perturbations such as long-period surface waves from distant earthquakes. Analyses of 31 Mw ≥ 6.0 teleseismic events show no evidence of dynamic triggering during the 2017 Changdao swarm, with peak dynamic stresses of 1.63 kPa (Supplementary Figure S10), which is far below typical triggering thresholds (~10 kPa)[97,98]. While a few β-statistic values exceeded the typical threshold of 2, the corresponding dynamic stresses were very small (less than 0.2 kPa) (Supplementary Figure S10) and no obvious instantaneous triggering was observed during the teleseismic surface waves (Supplementary Figures S11, S12), likely reflecting statistical fluctuations rather than genuine dynamic triggering[99,100]. These results further suggest that the swarm was internally driven by local fluid migration and fault-valve processes rather than remote seismic waves.

Our study investigates multiple observational datasets surrounding the Changdao swarm, leading us to suggest that the swarm may be associated with episodic reactivation of ancient basement faults driven by deep volatile-rich fluids in an intraplate setting. Multiple lines of independent evidence support this fluid-driven mechanism: positive ISO components (13-38%), higher b-values, high ETAS background forcing (~63%), a vertical low-V_P/V_S conduit, and CO_2-rich geochemical signatures. The spatiotemporal evolution of this fault-valve system, particularly its diffusivity variations (0.08 - 1.2 $m^2\ s^{-1}$) and migration patterns provided crucial insights into the underlying fluid dynamics. These findings reveal fluid-fault interaction as a primary control on swarm evolution and provide a framework for identifying and understanding similar fluid-induced seismicity globally. Future research will focus on the role of aseismic slip in such fluid-driven sequences investigating how the coupling between aseismic deformation and fluid pressure evolution controls the spatiotemporal patterns of earthquake swarms[101].

Methods

Matched Filter Event Detection and hypoDD Relocation

The analysis procedures largely follow the methodology[41] and are briefly summarized here. Continuous seismic waveforms were recorded by 19 stations within 150 km of the Changdao swarm (Figure 1), and each station equipped with broadband three-component instruments sampling at 100 Hz. For the matched filter event detection, we selected four stations (CHD, BHC, YTA, and LOK) within 100 km of the swarm. Additional stations were included for relocation and focal mechanism analysis (Figure 1). The continuous waveforms were band-pass filtered between 2 and 10 Hz. A total of 223 earthquakes ($M_L \geqslant 2.0$) were chosen as template events, using a 6-s window (1 s before and 5 s after the P- or S-wave arrival). Cross-correlation coefficients (CCCs) were computed with continuous waveforms from February 9 to May 31, 2017. Note that the Changdao earthquake swarm lasted from February 14 to August 2017. However, the location of the nearest seismic station (CHD) was shifted 4 km to the northwest on June 6 2017, which may affect the location accuracy. In addition, the earthquake intensity and frequency declined substantially after June. Hence in this study we only analyzed data between February 9 2017 and May 31 2017.

New events were detected when the CCC exceeded a threshold of 12 times the median absolute deviation (MAD). To avoid false detections, only one event was allowed within 5 s and selected based on the maximum CCC. The detected event's origin time was estimated assuming similar travel times to the corresponding template event, and magnitudes were determined by comparing the S-wave maximum amplitudes of the detected and template events within a 4-s window (2 s before and after the S-wave arrival)[41]. An example is shown in Supplementary Figure S1. Using this method, 11,411 events were detected (including 225 template earthquakes) (Figure 2; Supplementary Data 1).

The detected events were relocated using the double-difference method hypoDD [42]. Relative differential times were measured for similar waveforms recorded at the same station using cross-correlation techniques, achieving sub-sample precision[102,103]. Four additional stations (ZHY, LZH, YTA, WEH) were included in the relocation process (Figure 1). CCCs were calculated within a 3-s window starting 1 s before the P-wave arrival (vertical component) and S-wave arrival (horizontal components). The derived differential times and CCCs were used as input for hypoDD. Additional analysis steps and the error analyses[43] were from Yang et al. (2009).

We used a 1-D velocity model derived from seismic tomography[104] (Supplementary Table S2) with a V_P/V_S ratio of 1.72, which is standard for double-difference relocations in similar studies[22] and minimizes bias when combined with waveform cross-correlation[22]. Events with CCCs ≥0.8 and at least four differential station measurements were selected, resulting in 6,255 event pairs. In total, 2,142 events (18.8% of detected events) were successfully relocated (Supplementary Data 2).

Focal mechanism

Focal mechanisms were determined using P-wave first motions[48] for events with the magnitude between 2.0 and 3.4, and moment tensors were inverted for six M_L ⩾3.5 events using the Cut-and-Paste (CAP) method[47]. The same 1-D velocity model was used for ray tracing and Green's function computation. First-motion solutions were calculated for events with well-constrained locations and at least eight first motion polarities, events with over 10% inconsistent polarities were excluded. For CAP inversion, we selected stations with high-quality waveforms.

The inversion included isotropic and CLVD components. Optimal solutions were determined by minimizing residuals between observed and synthetic waveforms (Supplementary Figure S2). The frequency bands were 0.05-0.2 Hz for Pnl waves and 0.05-0.1 Hz for surface waves. Focal mechanism solutions were obtained for 185 earthquakes (M_L >2.0) (Supplementary Figure S4, Supplementary Data 3). We chose twelve focal mechanism solutions marked in Figure 3 and 4, representative earthquakes were selected based on three criteria: (1) events with magnitudes $M_L \geqslant 3.5$; (2) the largest event occurring each month during the swarm sequence; (3) the largest event along each distinct fault branch identified through seismicity distribution.

Fluid Diffusions from Migrating Seismicity

Earthquake migration patterns often reflect fluid diffusion processes, which can be described by the equation $r = \sqrt{4\pi Dt}$, where r is the distance from the injection point (assumed to be the initial event) to the seismicity front at time t, and D is the hydraulic diffusivity[53,57,58]. We fit the seismicity front by this diffusion equation, varying D value. Similarly, we referred to the estimated D as seismic diffusivity[58], encompassing mechanisms such as pore fluid diffusion and static stress triggering. Typical D values range from 10^{-2} to 10 m^2 s^{-1} for natural or induced earthquakes[31,52,59]. D values obtained in this study range from 0.08 to 1.2 m^2 s^{-1} (Figure 5).

Epidemic-Type Aftershock Sequence Modeling

To estimate the temporal evolution of fluid-induced seismicity, we applied the Epidemic-Type Aftershock Sequence (ETAS) model[63], which accounts for both background (fluid-driven) and triggered seismicity. The total occurrence rate $\lambda(t)$ is expressed as the sum of a time-varying forcing rate $\lambda_0(t)$ (representing background activity) and the rate of earthquakes triggered by all previous events:

$$\lambda(t) = \lambda_0(t) + \sum_{i:t_i<t} K_0\, e^{\alpha(M_i-M_c)}(t - t_i + c)^{-p} \qquad (1)$$

where, M_c is the completeness magnitude, and K_0, α, c, and p are parameters governing the triggering efficiency, magnitude dependence, and temporal decay of aftershocks. The specific inversion procedure[63] is briefly summarized here. The model parameters were estimated using an iterative algorithm: (1) an initial constant forcing rate λ_0 was assumed. (2) the ETAS parameters (K_0, α, c, and p) were estimated by minimizing the Akaike Information Criterion (AIC). (3) the forcing rate $\lambda_0(t)$ was updated by smoothing the probabilities ω_i that each event is a background event, using a moving window of $2n_e + 1$ events (n_e events before and after t_i). The optimal smoothing window was determined by minimizing AIC. (4) steps 2 and 3 were repeated until all parameters converged. The forcing rate and other ETAS parameters of the whole Changdao swarm were obtained with the minimum AIC at n_e=8, corresponding to a smoothing window of 17 events (Figure 6a). We also estimated forcing rate $\lambda_0(t)$ and other ETAS parameters for different periods (Figure 6b). In order to capture the temporal evolution of the forcing rate, we further estimated the time-dependent forcing rate $\lambda_0(t)$ and other ETAS parameters for distinct periods (Figure 6b), which correspond to different seismic activity stages of the earthquake sequence (Figure 2a). In particular, Stage II was divided into three subintervals separated by March 14 and April 8 (Figure 6b).

Calculation of Dynamic Stress Remotely Triggered Seismicity

To investigate potential teleseismic influences on the Changdao earthquake swarm, we calculated peak dynamic stresses and β-statistics for 31 global earthquakes with Mw ≥ 6.0 occurring within one month before and the swarm activity period, at epicentral distances greater than 1000 km, as sourced from the USGS earthquake catalog. Peak ground velocity (PGV) was directly measured from the recorded teleseismic surface waveforms. Dynamic stress σ (MPa) was computed with a shear modulus (G = 30 GPa), surface wave velocity (v_{surf}=3.5 km s^{-1}):

$$\sigma \approx G \frac{PGV}{v_{surf}} \quad (1)$$

To assess seismicity rate changes following teleseismic wave arrivals, we calculated the β-statistic, which is the most common statistic used in dynamic earthquake triggering studies, defined as[105]:

$$\beta = \frac{N_{post} - N_{pre}}{\sqrt{N_{pre}}} \quad (2)$$

Where, N_post is the number of earthquakes observed in a 3-day window post-arrival, and N_pre is the number in pre-window based on background seismicity rates. Elevated β values (β > 2) were identified to detect potential triggering, though these were further evaluated for spatial clustering and stress thresholds to distinguish teleseismic influences from background fluctuations[99].

To further investigate the instantaneous triggering effects of teleseismic surface waves on the Changdao region, we selected 12 Mw ⩾ 6.5 global earthquakes recorded by local stations near Changdao Island. Following previous studies[97,106,107,108], we applied a 5 Hz high-pass filter to the original waveforms of these teleseismic records. This filtering process suppresses the low-frequency teleseismic surface waves while amplifying signals from local small earthquakes. Consequently, any potential triggering phenomena would reveal previously obscured micro-earthquakes hidden beneath the large-amplitude surface waves. Additionally, spectrograms corresponding to the teleseismic waveform intervals were analyzed. These spectrograms clearly display the energy distribution across different frequencies upon the arrival of seismic waves: teleseismic energy is predominantly concentrated in the low-frequency band, whereas signals from local to regional earthquakes should show up in the relatively high-frequency band. Supplementary Figure S11 shows an example of the transverse T component from teleseismic waveforms of the maximum dynamic stress earthquake (1.63 Kpa, the Jan 22, 2017 Mw 7.9 Papua New Guinea event at ~6080 km). A few events occurred right following the P wave of the distant mainshock. These events mostly occurred near the Haicheng region, about 100-200 km away from the study region. Supplementary Figure S12 shows that one magnitude 1.8 event occurred during the surface waves of the Mar 29, 2017 M6.6 event near Ust'-Kamchatsk Staryy, Russia. A few additional events occurred following the distant seismic waves. However, the corresponding β values are -2.6 and -6.5 for 0.5 and 1 days, respectively, and the dynamic stress is only 1.02 KPa, well below triggering thresholds and inconsistent with a triggering interpretation. These events likely represent temporal coincidences with the teleseismic waves rather than genuine triggering.

Data availability

Three-component (3-C) waveform data from 12 seismic stations are available from the China Earthquake Network Center (CENC) Data Sharing Service (login required): https://data.earthquake.cn/datashare/login.jsp. The datasets supporting this study are deposited on Figshare (DOI: 10.6084/m9.figshare.30944375), including the detected earthquake catalogue (Supplementary Data 1), the relocated earthquake catalogue (Supplementary Data 2), and the focal-mechanism catalogue (Supplementary Data 3). The Figshare files are under embargo until 24 January 2026, after which they will be publicly accessible[45].

Code availability

ETAS modelling was implemented using GeoTaos[61] (https://bemlar.ism.ac.jp/lxl/). The MFT code[41] is also available from the corresponding author.

References

1. Ben-Zion, Y. & Sammis, C. G. Characterization of fault zones. *Pure Appl. Geophys.* **160**, 677–715 (2003). https://doi.org/10.1007/PL00012554

2. Wibberley, C. A., Gonzalez-Dunia, J. & Billon, O. Faults as barriers or channels to production-related flow: insights from case studies. *Pet. Geosci.* **23**, 134–147 (2017). https://doi.org/10.1144/petgeo2016-057

3. Xu, J. *et al*. Features of seismogenic structures of great earthquakes in the Bohai Bay basin area, north China. *Seismol. Geol.* **34**, 618–636 (2012).

4. Sibson, R. H. Conditions for fault-valve behaviour. *Geol. Soc. Lond. Spec. Publ.* **54**, 15–28 (1990).

https://doi.org/10.1144/GSL.SP.1990.054.01.02

5. Ruh, J. B. & Vergés, J. Effects of reactivated extensional basement faults on structural evolution of fold-and-thrust belts: insights from numerical modelling applied to the Kopet Dagh Mountains. *Tectonophysics* **746**, 493–511 (2018). https://doi.org/10.1016/j.tecto.2017.05.020

6. Sibson, R. H. An episode of fault-valve behaviour during compressional inversion?— The 2004 MJ6.8 Mid-Niigata Prefecture, Japan, earthquake sequence. *Earth Planet. Sci. Lett.* **257**, 188–199 (2007). https://doi.org/10.1016/j.epsl.2007.02.031

7. Kato, A. *et al.* Reactivation of ancient rift systems triggers devastating intraplate earthquakes. *Geophys. Res. Lett.* **36**, L05301 (2009). https://doi.org/10.1029/2008GL036450

8. Kato, A. Implications of fault-valve behavior from immediate aftershocks following the 2023 Mj6.5 earthquake beneath the Noto Peninsula, central Japan. *Geophys. Res. Lett.* **51**, e2023GL106444 (2024). https://doi.org/10.1029/2023GL106444

9. Peng, Z. *et al.* The evolution process between the earthquake swarm beneath the Noto Peninsula, central Japan and the 2024 M 7.6 Noto Hanto earthquake sequence. *Earthq. Res. Adv.* **100332** (2025). https://doi.org/10.1016/j.eqrea.2024.100332

10. Sibson, R. H. Structural permeability of fluid-driven fault-fracture meshes. *J. Struct. Geol.* **18**, 1031–1042 (1996). https://doi.org/10.1016/0191-8141(96)00032-6

11. Townend, J. & Zoback, M. D. How faulting keeps the crust strong. *Geology* **28**, 399–402 (2000). https://doi.org/10.1130/0091-7613(2000)28<399:HFKTCS>2.0.CO;2

12. Camanni, G. & Ye, Q. The significance of fault reactivation on the Wilson cycle undergone by the

northern South China Sea area in the last 60 Myr. *Earth-Sci. Rev.* **225**, 103893 (2022). https://doi.org/10.1016/j.earscirev.2021.103893

13. Ma, Z. *et al.* Slow rupture in a fluid-rich fault zone initiated the 2024 Mw 7.5 Noto earthquake. *Science* **385**, 866–871 (2024). https://doi.org/10.1126/science.ado5143

14. Sibson, R. H. Crustal stress, faulting and fluid flow. *Geol. Soc. Lond. Spec. Publ.* **78**, 69–84 (1994). https://doi.org/10.1144/GSL.SP.1994.078.01.07

15. Miller, S. A. The role of fluids in tectonic and earthquake processes. *Adv. Geophys.* **54**, 1–46 (2013). https://doi.org/10.1016/B978-0-12-380940-7.00001-9

16. Yoshida, K. *et al.* Updip fluid flow in the crust of the northeastern Noto Peninsula, Japan, triggered the 2023 Mw 6.2 Suzu earthquake during swarm activity. *Geophys. Res. Lett.* **50**, e2023GL106023 (2023). https://doi.org/10.1029/2023GL106023

17. Yoshida, K. *et al.* Role of a hidden fault in the early process of the 2024 Mw7.5 Noto Peninsula earthquake. *Geophys. Res. Lett.* **51**, e2024GL110993 (2024). https://doi.org/10.1029/2024GL110993

18. Mogi, K. Some discussions on aftershocks, foreshocks and earthquake swarms—the fracture of a semi finite body caused by an inner stress origin and its relation to the earthquake phenomena. *Bull. Earthq. Res. Inst.* **41**, 615–658 (1963).

19. Vidale, J. E. & Shearer, P. M. A survey of 71 earthquake bursts across southern California: exploring the role of pore fluid pressure fluctuations and aseismic slip as drivers. *J. Geophys. Res. Solid Earth* **111**, B05312 (2006). https://doi.org/10.1029/2005JB004034

20. Su, J., Lei, X., Li, J. & Huang, C. Detailed view of the seismogenic structures and processes of the 2022

Bayan Har intraplate earthquake swarm on the East Margin of the Qinghai–Tibet Plateau. *Seismol. Res. Lett.* **94**, 2167–2180 (2023). https://doi.org/10.1785/0220220336

21. Liu, M. *et al.* Intersection between tectonic faults and magmatic systems promotes swarms with large-magnitude earthquakes around the Tengchong volcanic field, southeastern Tibetan Plateau. *Geology* **52**, 302–307 (2024). https://doi.org/10.1130/G51796.1

22. Shelly, D. R., Moran, S. C. & Thelen, W. A. Evidence for fluid-triggered slip in the 2009 Mount Rainier, Washington earthquake swarm. *Geophys. Res. Lett.* **40**, 1506–1512 (2013). https://doi.org/10.1002/grl.50354

23. Shelly, D. R. *et al.* A fluid-driven earthquake swarm on the margin of the Yellowstone caldera. *J. Geophys. Res. Solid Earth* **118**, 4872–4886 (2013). https://doi.org/10.1002/jgrb.50362

24. Shelly, D. R. *et al.* Fluid-faulting interactions: fracture-mesh and fault-valve behavior in the February 2014 Mammoth Mountain, California, earthquake swarm. *Geophys. Res. Lett.* **42**, 5803–5812 (2015). https://doi.org/10.1002/2015GL064325

25. Ross, Z. E., Cochran, E. S., Trugman, D. T. & Smith, J. D. 3D fault architecture controls the dynamism of earthquake swarms. *Science* **368**, 1357–1361 (2020). https://doi.org/10.1126/science.abb0779

26. Lei, X. *et al.* Fault reactivation and earthquakes with magnitudes of up to Mw 4.7 induced by shale-gas hydraulic fracturing in Sichuan Basin, China. *Sci. Rep.* **7**, 7971 (2017). https://doi.org/10.1038/s41598-017-08557-y

27. Lei, X., Su, J. & Wang, Z. Growing seismicity in the Sichuan Basin and its association with industrial activities. *Sci. China Earth Sci.* **63**, 1633–1660 (2020). https://doi.org/10.1007/s11430-020-9646-x

28. Fischer, T. *et al.* Intra-continental earthquake swarms in West-Bohemia and Vogtland: a review.

Tectonophysics **611**, 1–27 (2014). https://doi.org/10.1016/j.tecto.2013.11.001

29. De Barros, L., Cappa, F., Deschamps, A. & Dublanchet, P. Imbricated aseismic slip and fluid diffusion drive a seismic swarm in the Corinth Gulf, Greece. *Geophys. Res. Lett.* **47**, e2020GL087142 (2020). https://doi.org/10.1029/2020GL087142

30. De Barros, L., Wynants-Morel, N., Cappa, F., & Danré, P. Migration of fluid-induced seismicity reveals the seismogenic state of faults. *J. Geophys. Res. Solid Earth* ***126***, e2021JB022767 (2021). https://doi.org/10.1029/2021JB022767

31. Shelly, D. R., Ellsworth, W. L. & Hill, D. P. Fluid-faulting evolution in high definition: connecting fault structure and frequency-magnitude variations during the 2014 Long Valley Caldera, California, earthquake swarm. *J. Geophys. Res. Solid Earth* **121**, 1776–1795 (2016). https://doi.org/10.1002/2015JB012719

32. Lei, X. & Wang, G. Is clustered seismicity an indicator of regional stress? Insights from earthquake sequences in Yongning-Luguhu faulted basin, Southwest China. *Earthq. Res. Adv.* **2**, 100138 (2022). https://doi.org/10.1016/j.eqrea.2022.100138

33. Woo, J. U. & Ellsworth, W. L. Reactivation of Precambrian faults by deep wastewater injection in Midland Basin, Texas, and performance evaluation of seismic response areas. *Bull. Seismol. Soc. Am.* **113**, 2543–2556 (2023). https://doi.org/10.1785/0120230086

34. Nishimura, T., Hiramatsu, Y. & Ohta, Y. Episodic transient deformation revealed by the analysis of multiple GNSS networks in the Noto Peninsula, central Japan. *Sci. Rep.* **13**, 8381 (2023). https://doi.org/10.1038/s41598-023-35459-z

35. Long, L., Kocaoglu, A., Hawman, R. & Gore, P. The Norris Lake earthquake swarm of June through

September, 1993; preliminary findings. *Seismol. Res. Lett.* **65**, 167–171 (1994). https://doi.org/10.1785/gssrl.65.2.167

36. Chen, J. & Wolf, L. W. A notable earthquake swarm in Alabama: natural or anthropogenic? *Seismol. Res. Lett.* **89**, 1583–1594 (2018). https://doi.org/10.1785/0220170284

37. Adeboboye, O. E. et al. Localized west-dipping seismic structure defines the Elgin-Lugoff Swarm Sequence in South Carolina. *Seismol. Res. Lett.* **95**, 123–145 (2024). https://doi.org/10.1785/0220240302

38. Li, X. *et al.* Inversion of P-wave three-dimensional velocity structure and analysis of seismogenic structure of earthquake swarm in 2017 in Miaodao islands, Shandong province. *Seismol. Geol.* **42**, 1188–1204 (2020).

39. Qu, J. *et al.* Crustal P-wave velocity structure and earthquake distribution in the Jiaodong Peninsula, China. *Tectonophysics* **814**, 228973 (2021). https://doi.org/10.1016/j.tecto.2021.228973

40. Gibbons, S. J. & Ringdal, F. The detection of low magnitude seismic events using array-based waveform correlation. *Geophys. J. Int.* **165**, 149–166 (2006). https://doi.org/10.1111/j.1365-246X.2006.02865.x

41. Peng, Z. & Zhao, P. Migration of early aftershocks following the 2004 Parkfield earthquake. *Nat. Geosci.* **2**, 877–881 (2009). https://doi.org/10.1038/ngeo697

42. Waldhauser, F. & Ellsworth, W. L. A double-difference earthquake location algorithm: method and application to the northern Hayward Fault, California. *Bull. Seismol. Soc. Am.* **90**, 1353–1368 (2000). https://doi.org/10.1785/0120000006

43. Yang, H. F., Zhu, L. P. & Chu, R. S. Fault-plane determination of the 18 April 2008 Mount Carmel, Illinois, earthquake by detecting and relocating aftershocks. *Bull. Seismol. Soc. Am.* **99**, 3413–3420 (2009).

https://doi.org/10.1785/0120090038

44. Wang, Z C. *et al.* Shallow-depth sonic reflection profiling studies on the active Penglai-Weihai fault zone offshore of the northern Shandong peninsula. *Chin. J. Geophys.*, **49**, 1092-1101 (2006). https://doi.org/10.1002/cjg2.920

45. Wang, P., Wang, B., Peng, Z. & Lei, X. The datasets of the 2017 Changdao swarm in eastern China. *figshare* (2026). https://doi.org/10.6084/m9.figshare.30944375

46. Wiemer, S. & Katsumata, K. Spatial variability of seismicity parameters in aftershock zones. *J. Geophys. Res. Solid Earth* **104**, 13135–13151 (1999). https://doi.org/10.1029/1999JB900032

47. Zhu, L. P. & Helmberger, D. V. Advancement in source estimation techniques using broadband regional seismograms. *Bull. Seismol. Soc. Am.* **86**, 1634–1641 (1996). https://doi.org/10.1785/BSSA0860051634

48. Yu, C. Q., Tao, K., Cui, X. F., Hu, X. P. & Ning, J. Y. P-wave first-motion focal mechanism solution and their quality evaluation. *Chin. J. Geophys.* **52**, 1402–1411 (2009).

49. Vavryčuk, V., & Hrubcová, P. Seismological evidence of fault weakening due to erosion by fluids from observations of intraplate earthquake swarms. *J. Geophys. Res. Solid Earth* ***122***, 3701-3718 (2017). https://doi.org/10.1002/2017JB013958

50. Vavryčuk, V. Iterative joint inversion for stress and fault orientations from focal mechanisms. *Geophys. J. Int.* **199**, 69–77 (2014). https://doi.org/10.1093/gji/ggu224

51. Liu, F. B., Qu, J. H., Li, G. Y. & Tian, Z. Y. Time-space evolution characteristics of the focal mechanism consistency parameter of the Changdao earthquake swarm in Shandong Province. *China Earthq. Eng. J.* **40**, 1034–1041 (2018).

52. Chen, X., Shearer, P. M. & Abercrombie, R. E. Spatial migration of earthquakes within seismic clusters in Southern California: evidence for fluid diffusion. *J. Geophys. Res.* **117**, B04301 (2012). https://doi.org/10.1029/2011JB008973

53. Shapiro, S. A., Huenges, E. & Borm, G. Estimating the crust permeability from fluid-injection-induced seismic emission at the KTB site. *Geophys. J. Int.* **131**, F15–F18 (1997). https://doi.org/10.1111/j.1365-246X.1997.tb01215.x

54. Lohman, R. B. & McGuire, J. J. Earthquake swarms driven by aseismic creep in the Salton Trough, California. *J. Geophys. Res. Solid Earth* **112**, B04405 (2007). https://doi.org/10.1029/2006JB004596

55. Peng, Z. & Lei, X. Physical mechanisms of earthquake nucleation and foreshock: cascade triggering, aseismic slip, or fluid flows? *Earthq. Res. Adv.* **5**, 100349 (2025). https://doi.org/10.1016/j.eqrea.2024.100349

56. Hainzl, S. Seismicity patterns of earthquake swarms due to fluid intrusion and stress triggering. *Geophys. J. Int.* **159**, 1090–1096 (2004). https://doi.org/10.1111/j.1365-246X.2004.02463.x

57. Shapiro, S. A., Rentsch, S. & Rothert, E. Characterization of hydraulic properties of rocks using probability of fluid-induced microearthquakes. *Geophysics* **70**, 27–33 (2005). https://doi.org/10.1190/1.1897030

58. Schoenball, M. & Ellsworth, W. L. A systematic assessment of the spatiotemporal evolution of fault activation through induced seismicity in Oklahoma and southern Kansas. *J. Geophys. Res. Solid Earth* **122**, 10189–10206 (2017). https://doi.org/10.1002/2017JB014850

59. Sheng, M. *et al.* Earthquakes triggered by fluid diffusion and boosted by fault reactivation in Weiyuan, China due to hydraulic fracturing. *J. Geophys. Res. Solid Earth* **127**, e2021JB022963 (2022).

https://doi.org/10.1029/2021JB022963

60. Yukutake, Y. *et al.* Fluid-induced swarm earthquake sequence revealed by precisely determined hypocenters and focal mechanisms in the 2009 activity at Hakone volcano, Japan. *J. Geophys. Res. Solid Earth* **116**, B04308 (2011). https://doi.org/10.1029/2010JB008036

61. Ogata, Y. Detection of precursory relative quiescence before great earthquakes through a statistical model, *J. Geophys. Res. Solid Earth* **97**, 19,845–19,871 (1992). https://doi.org/10.1029/92JB00708

62. Hainzl, S. & Ogata, Y. Detecting fluid signals in seismicity data through statistical earthquake modeling. *J. Geophys. Res.* **110**, B05S07 (2005). https://doi.org/10.1029/2004JB003247

63. Lei, X. *et al.* A detailed view of the injection-induced seismicity in a natural gas reservoir in Zigong, southwestern Sichuan basin, China. *J. Geophys. Res. Solid Earth* ***118***, 4296-4311, (2013). https://doi.org/10.1002/jgrb.50310

64. Zhang, H., Eaton, D. W., Li, G., Liu, Y. & Harrington, R. M. Discriminating induced seismicity from natural earthquakes using moment tensors and source spectra. *J. Geophys. Res. Solid Earth*, **121**, 972-993 (2016). https://doi.org/10.1002/2015JB012603

65. Lin, G., Peng, Z. & Neves, M. Comparisons of in situ V_P/V_S ratios and seismic characteristics between northern and southern California. *Geophys. J. Int.* **229**, 2162–2174 (2022). https://doi.org/10.1093/gji/ggac038

66. Sui, S., Shen, W., Mahan, K. & Schulte-Pelkum, V. Constraining the crustal composition of the continental US using seismic observables. *GSA Bull.* **135**, 2038–2056 (2023). https://doi.org/10.1130/B36229.1

67. Ji, G., Lei, J. & Zhao, D. 3-D crustal velocity structure and seismogenic environment of earthquake swarms in the Jiaodong area using multiple-phase travel-time tomography. *Chin. J. Geophys.* **68**, 123–138

(2025).

68. Lin, G. & Shearer, P. M. Evidence for water-filled cracks in earthquake source regions. *Geophys. Res. Lett.* **36**, L17315 (2009). https://doi.org/10.1029/2009GL039098

69. Lin, G. Spatiotemporal variations of in situ V_P/V_S ratio within the Salton Sea Geothermal Field, southern California. *Geothermics* **84**, 101740 (2020). https://doi.org/10.1016/j.geothermics.2019.101740

70. Nakajima, J. Crustal structure beneath earthquake swarm in the Noto Peninsula, Japan. *Earth Planets Space* **74**, 160 (2022). https://doi.org/10.1186/s40623-022-01719-x

71. Nakajima, J. The Wakayama earthquake swarm in Japan. *Earth Planets Space* 75, 48 (2023). https://doi.org/10.1186/s40623-023-01807-6

72. Okada, T. *et al.* Shear wave splitting and seismic velocity structure in the focal area of the earthquake swarm and their relation with earthquake swarm activity in the Noto Peninsula, Central Japan. *Earth Planets Space* **76**, 24 (2024). https://doi.org/10.1186/s40623-024-01974-0

73. Geoffroy, L. *et al.* Hydrothermal fluid flow triggered by an earthquake in Iceland. *Commun. Earth Environ.* **3**, 54 (2022). https://doi.org/10.1038/s43247-022-00382-0

74. Masihi, A. & Fischer, T. In-situ V_P/V_S ratio variations in seismic swarms as indicator of magmatic processes: Fagradalsfjall volcanic activity, SW Iceland. *Geophys. J. Int.* **241**, 1725–1739 (2025). https://doi.org/10.1093/gji/ggaf122

75. Huang, Y. *et al.* Fault material heterogeneity controls deep interplate earthquakes. *Sci. Adv.* **11**, eadr9353 (2025). https://doi.org/10.1126/sciadv.adr9353

76. Toksöz, M. N., Cheng, C. H. & Timur, A. Velocities of seismic waves in porous rocks. *Geophysics* **41**,

621–645 (1976). https://doi.org/10.1190/1.1440639

77. Takei, Y. Effect of pore geometry on V_P/V_S: from equilibrium geometry to crack. *J. Geophys. Res. Solid Earth* **107**, ECV 6-1–ECV 6-14 (2002). https://doi.org/10.1029/2001JB000522

78. Doi, I. *et al.* Relationship between hypocentral distributions and V_P/V_S ratio structures inferred from dense seismic array data: a case study of the 1984 western Nagano Prefecture earthquake, central Japan. *Geophys. J. Int.* **195**, 1323–1336 (2013). https://doi.org/10.1093/gji/ggt312

79. Ou, G.X. *et al.* Research progress on mantle fluids and deep oil and gas in the Miaodao Archipelago. In *China Geophysics 2010: Proceedings of the 26th Annual Meeting of the Chinese Geophysical Society and the 13th Academic Conference of the Seismological Society of China* 187–188 (Chinese Geophysical Society & Seismological Society of China, 2010).

80. Chen, C. et al. Mantle transition zone, stagnant slab and intraplate volcanism in Northeast Asia. *Geophys. J. Int.* **209**, 68–85 (2017). https://doi.org/10.1093/gji/ggw491

81. Lei, J., Tian, X., Mishra, O. P. & Huang, Z. Deep structure and dynamics under East Asia. *J. Asian Earth Sci.* **258**, 105921 (2023). https://doi.org/10.1016/j.jseaes.2023.105921

82. Xu, X. W., Wu, W. M. & Zhang, X. K. The latest tectonic changes and earthquakes in the crustal region of the capital region. (Science Press, Beijing, 2002).

83. Yu, X. F. *et al.* Deep structural framework and genetic analysis of gold concentration areas in the northwestern Jiaodong Peninsula, China: a new understanding based on high-resolution reflective seismic survey. *Acta Geol. Sin.* **92**, 1823–1840 (2018). https://doi.org/10.1111/1755-6724.13679

84. Sibson, R. H. Implications of fault-valve behaviour for rupture nucleation and recurrence. *Tectonophysics*

211, 283–293 (1992). https://doi.org/10.1016/0040-1951(92)90065-e

85. Gudmundsson, A., Marinoni, L. B. & Marti, J. Injection and arrest of dykes: implications for volcanic hazards. *J. Volcanol. Geotherm. Res.* **88**, 1–13 (1999). https://doi.org/10.1016/S0377-0273(98)00107-3

86. Chen, Y., Li, Z. H., Tang, K. & Shi, Y. Mechanism of metamorphic fluid expulsion from ductile contact aureole: insights from numerical modeling of a growing mid-crustal magma chamber. *Earth Planet. Sci. Lett.* **626**, 118545 (2024). https://doi.org/10.1016/j.epsl.2023.118545

87. Li, Y., Li, H. & Huang, Y. Seismicity in the Weiyuan-Rongxian area, Sichuan Basin, SW China. *J. Asian Earth Sci.* **272**, 106241 (2024). https://doi.org/10.1016/j.jseaes.2024.106241

88. Wang, P. & Wang, B. S. Stress drop estimation of Chang Island earthquake swarm by generalized superposition inversion method. *Chin. J. Geophys.* **63**, 1970–1985 (2020). https://doi.org/10.6038/cjg2020N0158

89. Cappa, F. Modelling fluid transfer and slip in a fault zone when integrating heterogeneous hydromechanical characteristics in its internal structure. *Geophys. J. Int.* **178**, 1357–1362 (2009). https://doi.org/10.1111/j.1365-246X.2009.04291.x

90. Cardenas, M. B. & Jiang, X.-W. Groundwater flow, transport, and residence times through topography-driven basins with exponentially decreasing permeability and porosity. *Water Resour. Res.* **46**, W11538 (2010). https://doi.org/10.1029/2010WR009370

91. Saar, M. O. & Manga, M. Depth dependence of permeability in the Oregon Cascades inferred from hydrogeologic, thermal, seismic, and magmatic modeling constraints. *J. Geophys. Res. Solid Earth* **109**, B04204 (2004). https://doi.org/10.1029/2003JB002855

92. Stober, I. Depth- and pressure-dependent permeability in the upper continental crust: data from the Urach 3 geothermal borehole, southwest Germany. *Hydrogeol. J.* **19**, 685–699 (2011). https://doi.org/10.1007/s10040-011-0704-7

93. Amezawa, Y. *et al*. Long-living earthquake swarm and intermittent seismicity in the northeastern tip of the Noto Peninsula, Japan. *Geophys. Res. Lett.* **50**, e2022GL102670 (2023). https://doi.org/10.1029/2022GL102670

94. Lei, X. Fluid-driven fault nucleation, rupture processes, and permeability evolution in Oshima granite-preliminary results and acoustic emission datasets. *Geohazard Mech.* **2**, 164–180. (2024). https://doi.org/10.1016/j.ghm.2024.04.003

95. van der Elst, N. J. & Brodsky, E. E. Connecting near-field and far-field earthquake triggering to dynamic strain. *J. Geophys. Res. Solid Earth*. **115**. B07311 (2010). https://doi.org/10.1029/2009JB006681

96. Bell, A.F. *et al.* Dynamic earthquake triggering response tracks evolving unrest at Sierra Negra volcano, Galápagos Islands. *Sci. Adv.* **7**, eabh0894 (2021). https://doi.org/10.1126/sciadv.abh0894

97. Hill, D. P. & Prejean, S. G. Dynamic Triggering. in Treatise on Geophysics 273–304 (Elsevier, 2015). https://doi.org/10.1016/B978-0-444-53802-4.00078-6.

98. Kilb, D., Gomberg, J. & Bodin, P. Triggering of earthquake aftershocks by dynamic stresses. *Nature* **408**, 570–574 (2000). https://doi.org/10.1038/35046046

99. Pankow, K. L. & Kilb, D. Going Beyond Rate Changes as the Sole Indicator for Dynamic Triggering of Earthquakes. *Sci. Rep.* **10**, 4120 (2020). https://doi.org/10.1038/s41598-020-60988-2

100. Hardebeck, J. L., DeSalvio, N. D., Fan, W., & Barbour, A. J. False positives in the identification of

dynamic earthquake triggering. *J. Geophys. Res. Solid Earth* **130**, e2025JB031566 (2025). https://doi.org/10.1029/2025JB031566

101. Danré, P., De Barros, L., Cappa, F. & Passarelli, L. Parallel dynamics of slow slips and fluid-induced seismic swarms. *Nat. Commun.* **15**, 8943 (2024). https://doi.org/10.1038/s41467-024-53285-3

102. Poupinet, G., Ellsworth, W. L. & Frechet, J. Monitoring velocity variations in the crust using earthquake doublets: an application to the Calaveras Fault, California. *J. Geophys. Res. Solid Earth* **89**, 5719–5731 (1984). https://doi.org/10.1029/JB089iB07p05719

103. Shearer, P. M. Improving local earthquake locations using the L1 norm and waveform cross correlation: application to the Whittier Narrows, California, aftershock sequence. *J. Geophys. Res. Solid Earth* **102**, 8269–8283 (1997). https://doi.org/10.1029/96JB03228

104. Pan, S. Z. *et al.* Crustal velocity structure beneath Jiaodong Peninsula and its tectonic implications. *Chin. J. Geophys.* **58**, 3251–3263 (2015). https://doi.org/10.6038/cjg20150920

105. Matthews, M. V. & Reasenberg, P. A. Statistical methods for investigating quiescence and other temporal seismicity patterns. *Pure Appl. Geophys.* **126**, 357–372 (1988). https://doi.org/10.1007/BF00879003

106. Peng, Z., Wang, W., Chen, Q.F. and Jiang, T. Remotely triggered seismicity in north China following the 2008 Mw 7.9 Wenchuan earthquake. *Earth Planets Space* **62**, 893–898 (2010). https://doi.org/10.5047/eps.2009.03.006.

107. Peng, Z., Long, L.T. and Zhao, P. The relevance of high-frequency analysis artifacts to remote triggering. *Seismol. Res. Lett.* **82**, 654–660 (2011). https://doi.org/10.1785/gssrl.82.5.654

108. Liu, G. *et al.* Detecting remotely triggered microseismicity around Changbaishan Volcano following

nuclear explosions in North Korea and large distant earthquakes around the world. *Geophys. Res. Lett.* **44**, 4829–4838 (2017). https://doi.org/10.1002/2017GL072511.

109. Wessel, P. *et al.* The Generic Mapping Tools version 6. *Geochem. Geophys. Geosyst.* **20**, 5556–5564 (2019). https://doi.org/10.1029/2019GC008515

Acknowledgments

We thank the CEE editors Dr. Luca Dal Zilio and Dr. Joe Aslin, reviewers Dr. Debi Kilb and another anonymous reviewer for their help in improving the manuscript, Dr. Hongfeng Yang for sharing his modified double difference location program, Drs Jianchang Zheng, Jinxi Hou, Bo Zhang for their suggestions on the focal source mechanisms, the matched-filter, and earthquake locations, respectively. This study was supported by the National Natural Science Foundation of China (Grant No. 42430103), Chinese Academy of Sciences (CAS) Project for Young Scientists in Basic Research (Grant No. YSBR-020), the Natural Science Foundation of Shandong Province, China (Grant No. ZR2024MD093), the Natural Science Foundation of Dongying city, the Scientific Research Startup Foundation of Shandong Institute of Petroleum and Chemical Technology (Grant No. 2024ZR032), and the Science Development Foundation of Dongying city, China (Grant No. DJB2022015). Z. P. is partially supported by the U.S. National Science Foundation (Grant No. RISE-2425889). Seismic waveforms and catalog are provided by the China Earthquake Networks Center. Figures are constructed with the Generic Mapping Tools[109].

Author contributions

P.W. and B.W. conceived and initiated the study. P.W. processed the data and drafted the manuscript. Z.P. provided the matched-filter detection code. B.W., Z.P., and X.L. contributed to interpretation of the results and revised the manuscript. P.W. prepared the figures and movie, with input and modifications suggested by Z.P., B.W., and X.L. The supplementary Movie was edited and refined by Z.P. All authors reviewed and approved the final manuscript.

Competing interests

The authors declare no competing interests.

Figure captions

Figure 1. The spatio-temporal evolution of the 2017 Changdao earthquake swarm.

(a) Map of seismicity and seismic stations in the study region. Red, blue, and cyan circles are earthquakes recorded by the China Earthquake Networks Center (CENC) during earthquake swarms in 2017, 2013, and 1976, respectively. The yellow star indicates the largest M_L4.5 earthquake in the 2017 swarm with its focal mechanism (red beach ball). The gray circle marks the largest historic earthquake in 1548 with a magnitude of 7.0. Triangles are seismic stations, and blue triangles mark stations used for matched filter event detection. Brown lines mark the surface traces of major faults from Wang et al. (2006) [44]. The inset indicates the study region (blue box) in a larger map of East Asia, and the black dashed lines are the two major faults: Zhangjiakou-Penglai Fault and Tan-Lu Fault. (b) Magnitudes versus the occurrence times and the cumulative numbers of all earthquakes within 40 km of Changdao Island since 1970.

Figure 2. Temporal evolution and frequency–magnitude characteristics of the Changdao swarm.

(a) Magnitudes and cumulative numbers versus time of the MFO (blue dots, N=11,411) and CENC (red dots, N=1804) catalogs. (b) Frequency-magnitude distribution of the MFO (blue), the MFR (black, N=2142), and the CENC (red) catalogs. The estimated magnitudes of completeness (Mc) calculated by the maximum curvature method of the MFO and the CENC catalogs are 0.8 and 1.1, respectively.

Figure 3. Spatio-temporal distribution of the Changdao earthquake swarm.

Hypocenter dots are colored by occurrence time relative to the initial event (2017-02-14 00:05:58 M_L1.2; marked as a black triangle). (a) Map view of all MFR events. The focal mechanism solutions of twelve representative earthquakes were marked. The magenta solid line indicates the mapped major (Penglai-Weihai) fault. The orientation of the regional stress field was marked on the top right. The black star indicates the largest M_L4.5 earthquake. The red and two dashed white parallelograms mark the central region (CR) and southeast and northwest regions (SR and NR). (b) and (c) are side views along profiles XX' and YY', respectively. The red and magenta lines in (b) indicate interpreted primary and secondary faults, respectively. PW: Penglai-Weihai. (d) A zoom-in view corresponding to the red box in (c). The red arrow marks the migration direction.

Figure 4. A 3D view of the relocated seismicity in the Changdao earthquake swarm.

The 3D view illuminates the complex fault structures. Black/dotted lines highlight the fault segments. The magenta arrow indicates the direction of earthquake migration in the fault intersection.

Figure 5. Spatiotemporal migration of seismicity relative to the first event.

The distance of seismicity relative to the first earthquake as a function of time for the entire region (a), the central (b), northwest (c), and southeast regions (d). The red lines were the fitted line with the sqrt(t) function ($r = \sqrt{4\pi Dt}$). The red dotted ellipse marks a swarm-like cluster with spatiotemporal concentration. The black curve in (a) marks the cumulative number of events over time.

Figure 6. ETAS results of the Changdao swarm.

(a) the forcing rate λ_0(t) for the whole period (n_e=8, corresponding to a smoothing window of 17 events). (b) the forcing rate λ_0(t) for different distinct periods. The f.s. indicates the forced seismicity. The initial and final periods stand for Stage I and Stage III in Figure 2a, respectively. The three middle periods corresponded to Stage II in Figure 2a.

Figure 7. V_P/V_S structure beneath the Changdao earthquake swarm.

(a) Diagram showing the V_P/V_S profiles and the hypocentral locations of the Changdao swarm. The white dotted circle marks the relatively low V_P/V_S area, and red arrows mark the upwelling hydrothermal fluid with CO_2 from deeper areas. (b) The location of cross-section profile in (a).

Editorial summary:

A distinctive migration pattern consistent with fluid pressure diffusion is identified within a high-resolution earthquake catalogue of the 2017 Changdao swarm and suggests a fault-valve mechanism driven by overpressure CO_2-rich fluids was responsible.

Peer review information:

Communications Earth and Environment thanks Debi Kilb and the other, anonymous, reviewer(s) for their contribution to the peer review of this work. Primary Handling Editors: Luca Dal Zilio and Joseph Aslin. [A peer review file is available.]

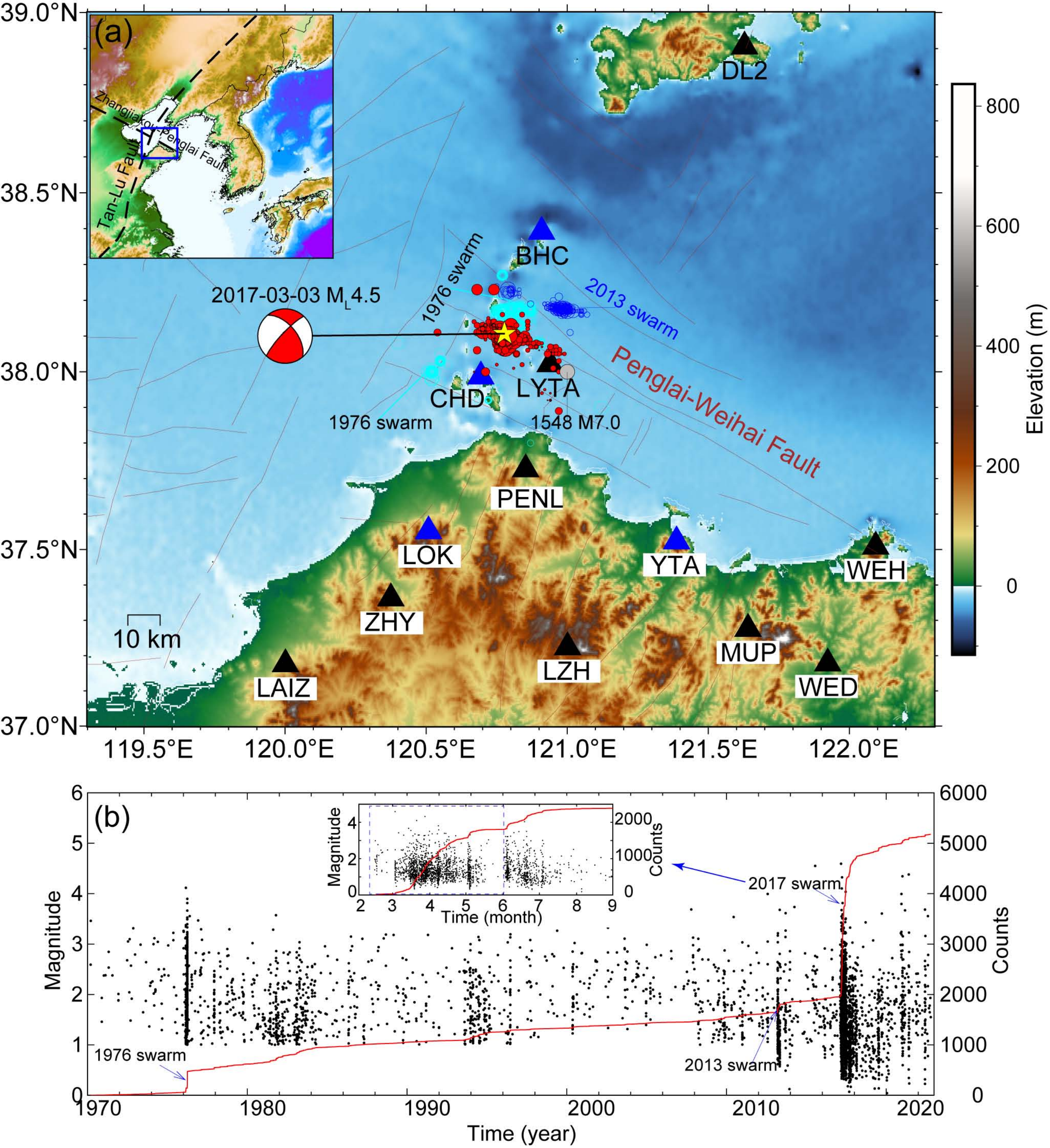
(a)
39.0°N
38.5°N
38.0°N
37.5°N
37.0°N
119.5°E
120.0°E
120.5°E
121.0°E
121.5°E
122.0°E
Zhangjiakou-Penglai Fault
Tan-Lu Fault
DL2
BHC
2017-03-03 M$_L$4.5
1976 swarm
2013 swarm
CHD
LYTA
1976 swarm
1548 M7.0
Penglai-Weihai Fault
PENL
LOK
YTA
WEH
ZHY
10 km
LZH
MUP
WED
LAIZ
Elevation (m)
800
600
400
200
0
(b)
Magnitude
Counts
Time (month)
2017 swarm
2013 swarm
1976 swarm
Time (year)
1970
1980
1990
2000
2010
2020

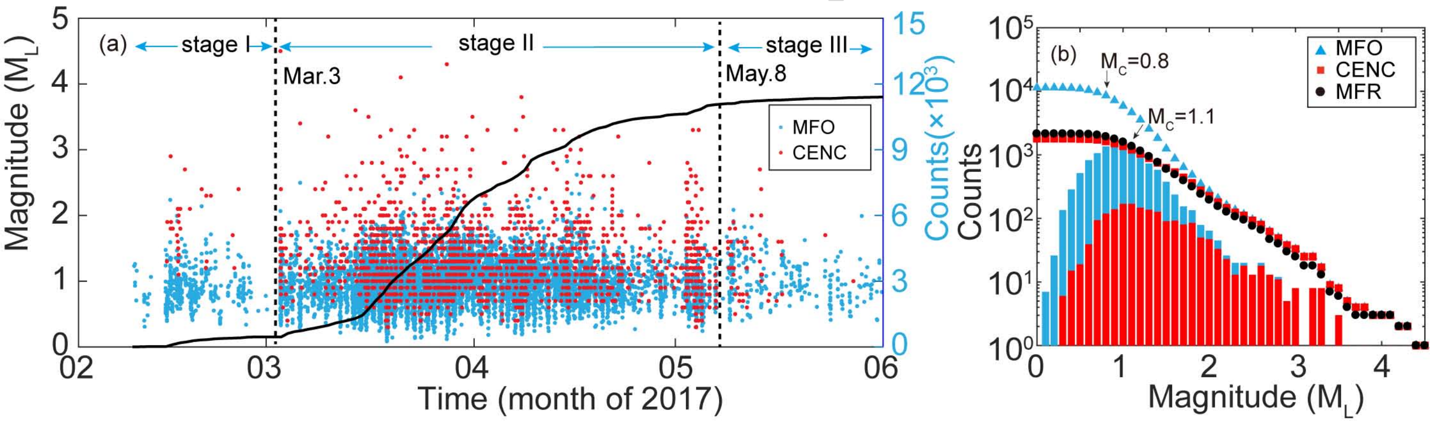
(a)
stage I
stage II
stage III
Mar.3
May.8
MFO
CENC
Magnitude (M_L)
Counts($\times 10^3$)
Time (month of 2017)
02
03
04
05
06
(b)
M_C=0.8
M_C=1.1
MFO
CENC
MFR
Counts
Magnitude (M_L)

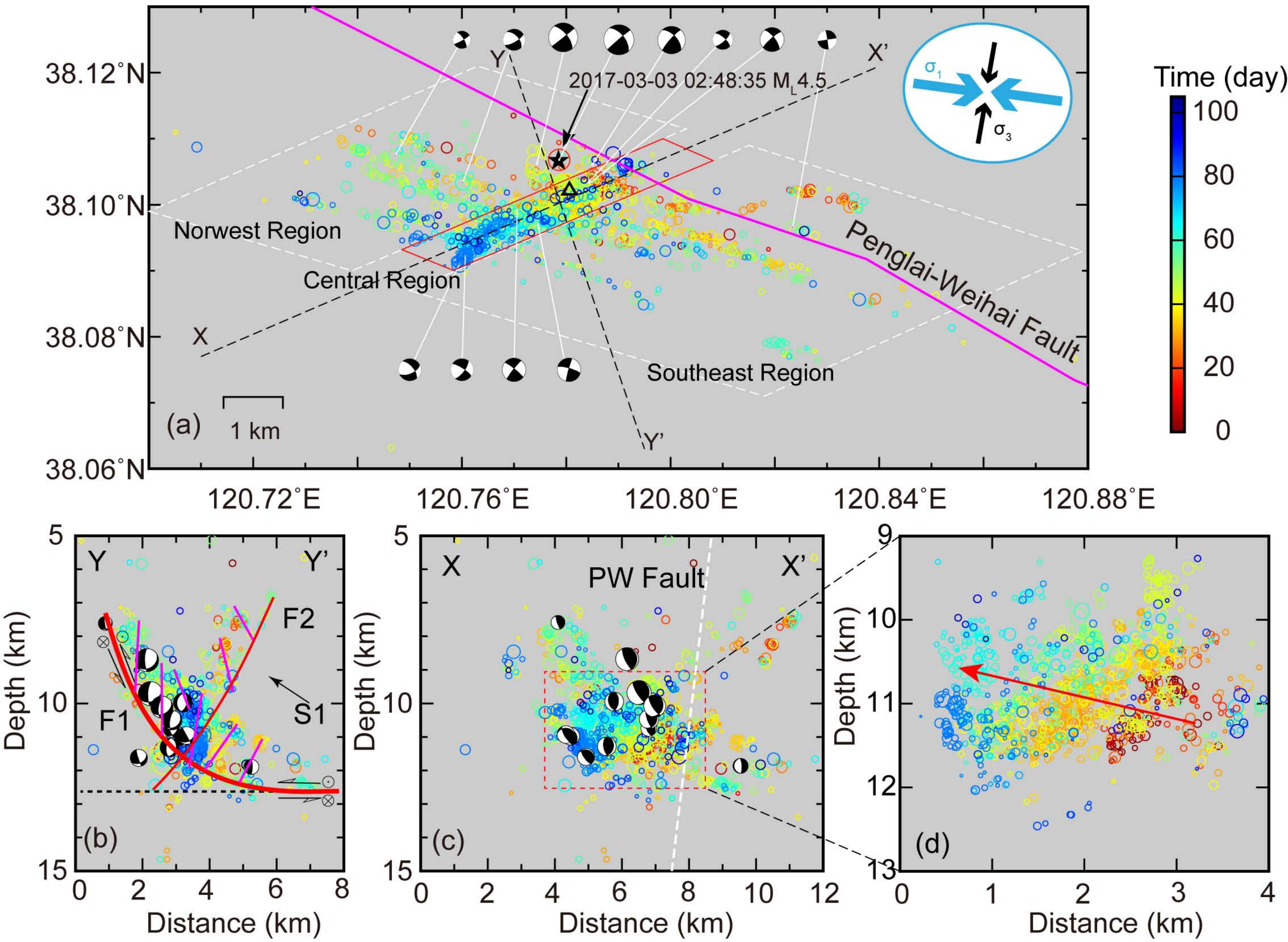
38.12°N
38.10°N
38.08°N
38.06°N
120.72°E
120.76°E
120.80°E
120.84°E
120.88°E
2017-03-03 02:48:35 M_L 4.5
Y
Y'
X
X'
Norwest Region
Central Region
Southeast Region
Penglai-Weihai Fault
(a)
1 km
σ1
σ3
Time (day)
100
80
60
40
20
0
Y
Y'
F1
F2
S1
(b)
Depth (km)
Distance (km)
X
X'
PW Fault
(c)
(d)

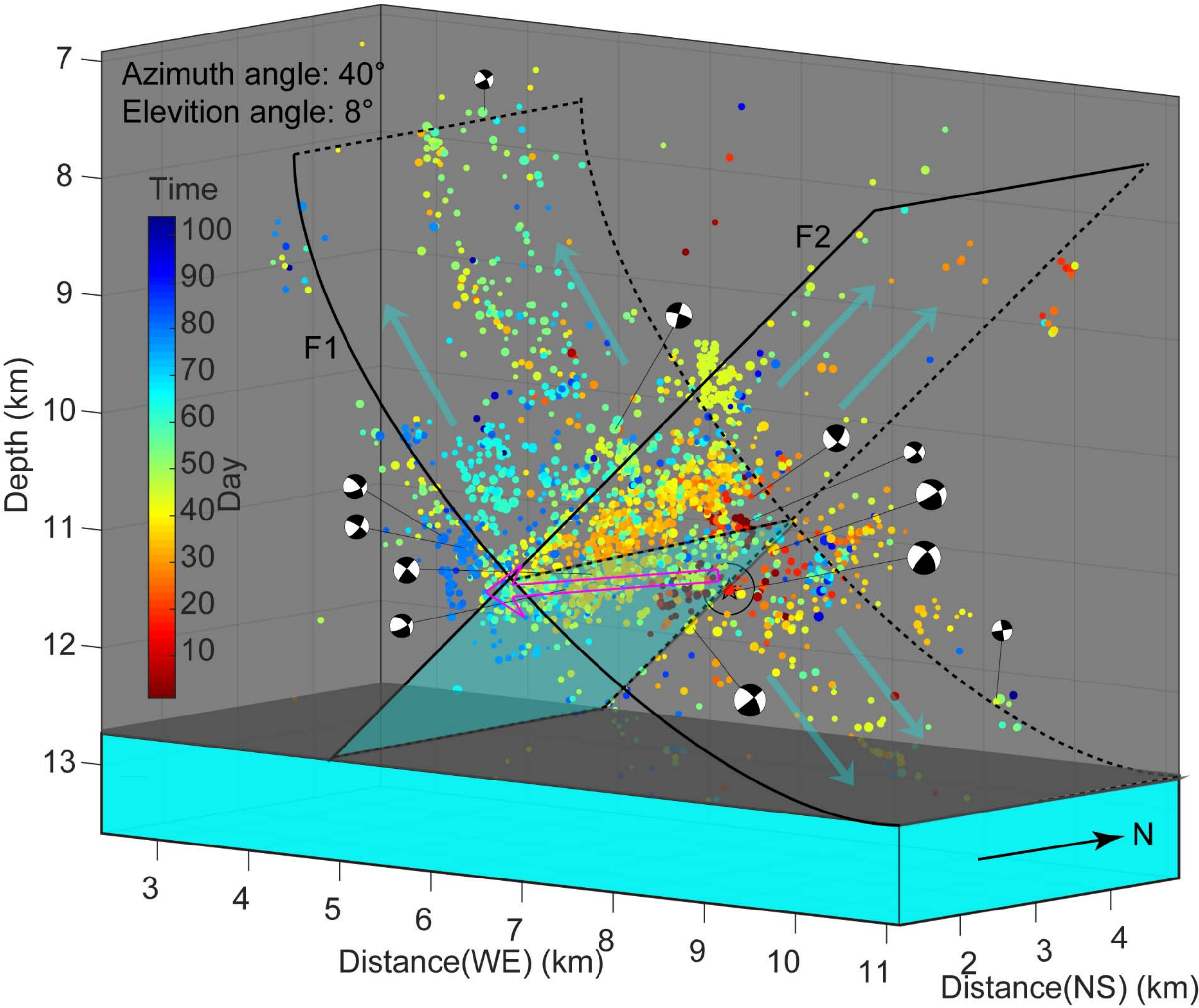
Azimuth angle: 40°
Elevition angle: 8°
Time
Day
100
90
80
70
60
50
40
30
20
10
F1
F2
N
Depth (km)
7
8
9
10
11
12
13
Distance(WE) (km)
3
4
5
6
7
8
9
10
11
Distance(NS) (km)
2
3
4

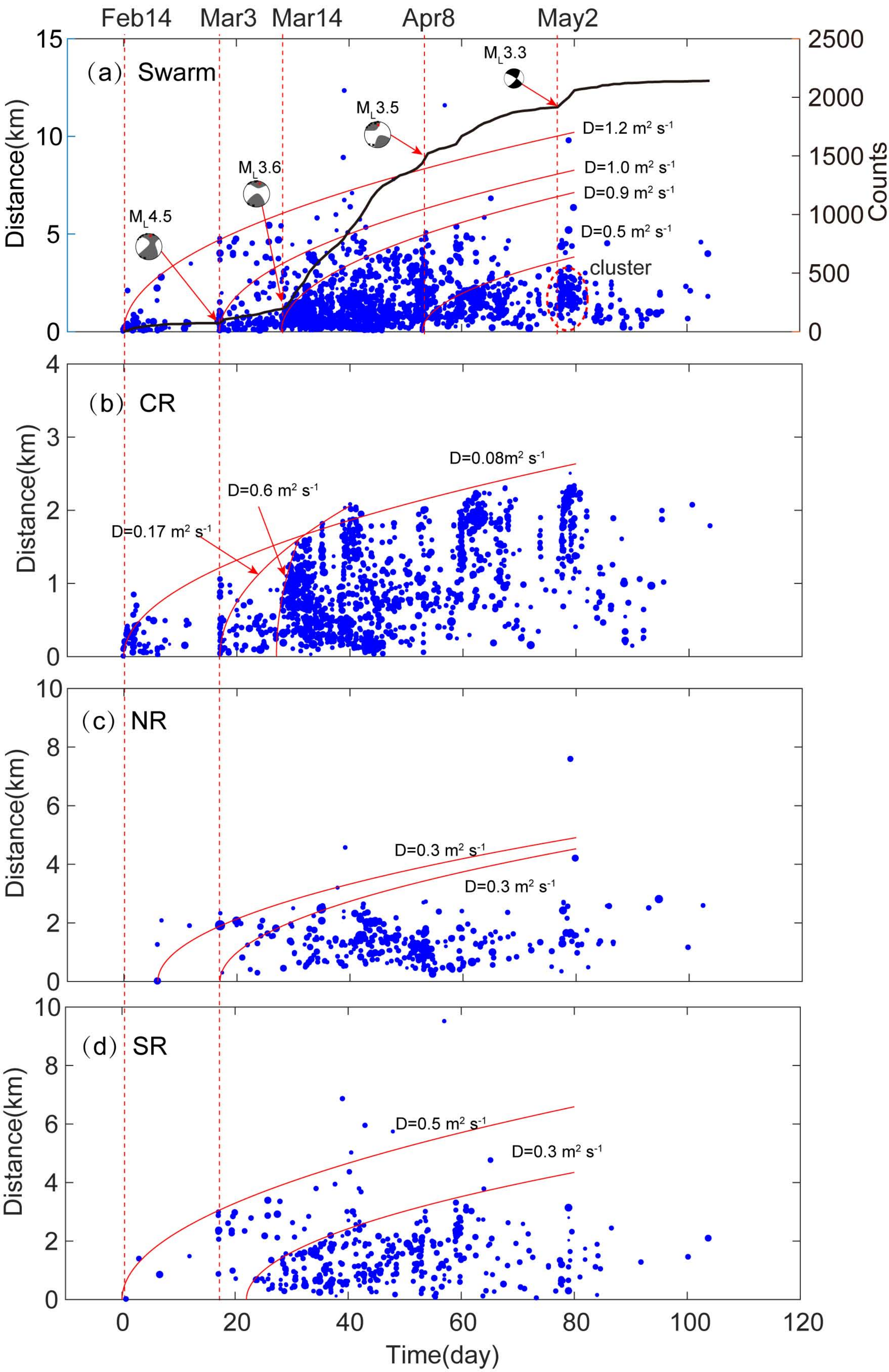
Feb14
Mar3
Mar14
Apr8
May2
(a) Swarm
M_L4.5
M_L3.6
M_L3.5
M_L3.3
D=1.2 m² s⁻¹
D=1.0 m² s⁻¹
D=0.9 m² s⁻¹
D=0.5 m² s⁻¹
cluster
Distance(km)
Counts
(b) CR
D=0.08m² s⁻¹
D=0.6 m² s⁻¹
D=0.17 m² s⁻¹
Distance(km)
(c) NR
D=0.3 m² s⁻¹
D=0.3 m² s⁻¹
Distance(km)
(d) SR
D=0.5 m² s⁻¹
D=0.3 m² s⁻¹
Distance(km)
Time(day)

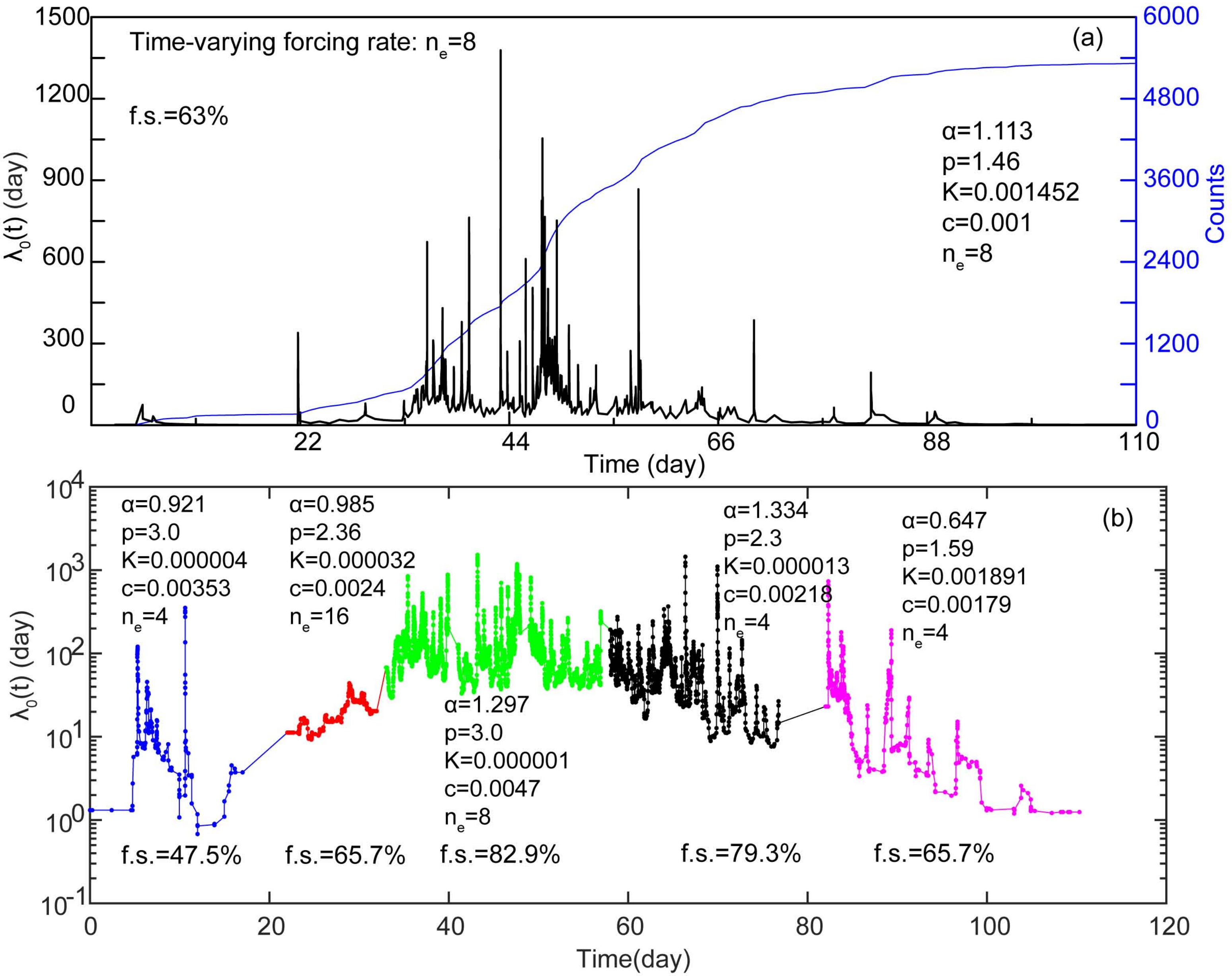

Time-varying forcing rate: ne=8
(a)
f.s.=63%
α=1.113
p=1.46
K=0.001452
c=0.001
ne=8
λ0(t) (day)
Counts
Time (day)
(b)
α=0.921
p=3.0
K=0.000004
c=0.00353
ne=4
α=0.985
p=2.36
K=0.000032
c=0.0024
ne=16
α=1.297
p=3.0
K=0.000001
c=0.0047
ne=8
α=1.334
p=2.3
K=0.000013
c=0.00218
ne=4
α=0.647
p=1.59
K=0.001891
c=0.00179
ne=4
f.s.=47.5%
f.s.=65.7%
f.s.=82.9%
f.s.=79.3%
f.s.=65.7%
λ0(t) (day)
Time(day)

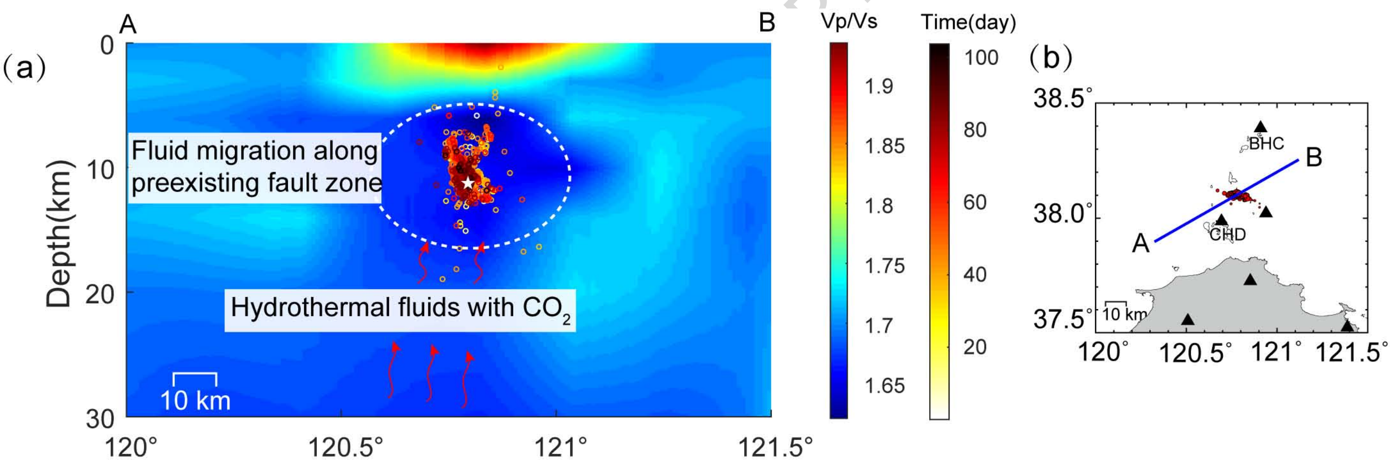
(a)
A
B
Vp/Vs
Time(day)
Depth(km)
Fluid migration along preexisting fault zone
Hydrothermal fluids with CO_2
10 km
0
10
20
30
120°
120.5°
121°
121.5°
1.9
1.85
1.8
1.75
1.7
1.65
100
80
60
40
20
(b)
38.5°
38.0°
37.5°
BHC
CHD
A
B
10 km
120°
120.5°
121°
121.5°